2. L. M. Liz-Marzán, M. Giersig and P. Mulvaney: *Langmuir*, 1996, **12**, 4329–4335.
3. M. Giersig, L. M. Liz-Marzán, T. Ung, D. Su and P. Mulvaney: *Ber. Bunsen-Ges. Phys. Chem.*, 1997, **101**, 1617–1620.
4. Y. Kobayashi, K. Misawa, M. Takeda, M. Kobayashi, M. Satake, Y. Kawazoe, N. Ohuchi, A. Kasuya and M. Konno: *Colloids Surf. A*, 2004, **251A**, 197–201.
5. Y. Kobayashi, K. Misawa, M. Takeda, M. Kobayashi, M. Satake, Y. Kawazoe, N. Ohuchi, A. Kasuya and M. Konno: Proc. 12th Int. Conf. Composites/Nano Eng. (ICCE-12) on 'Silica-coating of AgI nanoparticles using a modified Stöber method', Tenerife, Spain, August 2005, University of New Orleans.
6. Y. Kobayashi, K. Misawa, M. Takeda, N. Ohuchi, A. Kasuya and M. Konno: Proc. 4th Int. Conf. Adv. Mater. Process. (ICAMP-4) on 'Control of shell thickness in silica-coating of AgI nanoparticles', Hamilton, New Zealand, December 2006, The University of Waikato, 033.
7. Y. Sakurai, M. Takeda, Y. Kawazoe, A. Kasuya, Y. Kobayashi, T. Kamei, M. Nakajima and N. Ohuchi: *Breast Dis.*, 2006, **25**, 55–56.
8. W. Stöber, A. Fink and E. Bohn: *J. Colloid Interface Sci.*, 1968, **26**, 62–69.
9. S. C. Mitchell and A. Q. Zhang: *Clin. Chim. Acta*, 2001, **312**, 107–114.
10. R. Benigni and L. Passerini: *Mutat. Res.*, 2002, **511**, 191–206.
11. H. Vogelsang, O. Husberg and W. von der Osten: *J. Lumin.*, 2000, **86**, 87–94.
12. S. Kondo, T. Itoh and T. Saito: *Phys. Rev. B*, 1998, **57B**, 13235–13240.
13. P. S. Kumar, P. B. Dayal and C. S. Sunandana: *Thin Solid Films*, 1999, **357**, 111–118.
14. Y. Wang, J. Mo, W. Cai, L. Yao and L. Zhang: *Mater. Lett.*, 2002, **56**, 502–506.

Copyright © 2008 American Scientific Publishers
All rights reserved
Printed in the United States of America

Journal of
Nanoscience and Nanotechnology
Vol. 8, 1–8, 2008

Ultra-Stable Nanoparticles in $A_{II}B_{VI}$ (A_{II} = Cd, Zn; B_{VI} = S, Se, Te) Compounds

V. R. Romanyuk[1, †, *], I. M. Dmitruk[1, ‡], Yu. A. Barnakov[1], R. V. Belosludov[2], and A. Kasuya[1]

[1] Center for Interdisciplinary Research, Tohoku University, Sendai, 980-8578, Japan
[2] Institute for Materials Research, Tohoku University, Sendai, 980-8577, Japan

Laser ablation on binary $A_{II}B_{VI}$ compounds exhibits in time-of-flight mass spectra abundant peaks at stoichiometric $(A_{II}B_{VI})_n$ with $n = 13$, 19, 33 and 34 measured on bulk powders of CdSe, CdS, CdTe, ZnS and ZnSe. Investigation on solution grown nanometer size particles of CdSe shown an existence of ultra-stable stoichiometric clusters $(CdSe)_{13}$, $(CdSe)_{19}$, $(CdSe)_{33}$, $(CdSe)_{34}$ and $(CdSe)_{48}$. This set of n has not been predicted as particularly stable particles in previous bulk fragment models based on either zinc-blende or wurtzite, and a different type of structures is required to explain our experimental results. Present investigation shows that nanoparticles formed in vacuum as magic numbers above are found in solution as preferentially grown species in CdSe, and possibly in other $A_{II}B_{VI}$. It is suggested that the high stability of the observed magic clusters originates from their specific structure as endohedral binary fullerenes, supposedly. These molecular-like particles composed of few tens of atoms lie between atom and solid, and exhibit novel materials functions not realizable in the bulk.

Keywords: II–VI Compound Nanoparticles, Mass Spectra, Magic Numbers, Endohedral Structure, Closed Shell.

RESEARCH ARTICLE

1. INTRODUCTION

Nanostructured materials attract much of our attention as an intermediate phase between molecule and solid to explore fundamental aspects and possible applications in nano-electronic, biomedical and catalytic devices. Their extremely strong size and shape dependent structures in atomic scale[1–4] may lead to functional properties not realized in other forms of condensed matter. Nanoparticles of semiconductors have been particularly studied during the last decade in binary II–VI compounds,[5, 6] CdS,[7–10] CdSe[2, 3, 11, 12] and CdTe,[13–15] and their core–shell combinations with III–V, InAs/CdSe and InAs/InP,[16] because of recent advances in preparing high quality samples in solution. These nanoparticles, however, are mostly grown in diameters larger than 2 nm, and their structures are essentially of the bulk.

Particles of less than 1 nm are prepared more readily in vapor produced by thermal evaporation or laser ablation in vacuum. Martin[1] shows in his extensive mass spectral analysis, especially in metallic elements that small particles may have structures characterized by a concept of shell periodicity that is entirely different from the translational ones in bulk crystals. Similarly to shell structures in atoms and nuclei, the particle becomes particularly stable at the number of constituent atoms/molecules, n, that coincides with values called magic number to close the periodic shell. In mass spectra, stable magic number particles appear as abundant peaks relative to those of neighboring masses. The observed spectra further show that this shell periodicity exhibits a transition from "shells of electrons" to "shells of atoms." In Na_n, for example, this transition is noted at $n \sim 1{,}500$ as a discontinuity in periodicity represented by the sequence of magic numbers. It occurs because the origin to determine the stability of particle switches from the electronic state for $n < 1{,}500$, to the atomic arrangement for $n > 1{,}500$. The stable structures in both sides are still symmetrically different from the bulk of translational periodicity appearing at much larger sizes.[1, 17]

Comparing with metals, very few works have been reported on nanoparticles in semiconductor compounds with $n > 20$ partly because of difficulty in obtaining high yield of vapor to condense into larger particles. Previous works in ZnS as a binary $A_{II}B_{VI}$ compound (A_{II} = Cd, Zn; B_{VI} = S, Se, Te) find stoichiometric $(ZnS)_n$ that are

*Author to whom correspondence should be addressed.
†Present address: Institute for Physics of Semiconductors NAS of Ukraine, Prospect Nauki 41, Kyiv, 03028 Ukraine.
‡Permanent address: Physics Department, Kyiv Taras Shevchenko University, Kyiv, 03127 Ukraine.

abundant in $n < 35$.[1-18] Other binary systems of smaller ones are extensively studied, including Al_nS_n (Ref. [19]) and Te_nS_m.[20]

Small systems have much more freedom and flexibility than the bulk solid to adopt structures that would lower their free energy by changing dimensionality and morphology with atomic arrangements not possible in crystals.[3,6,21] Calculation on BN by Seifert,[22] for example, predicts that cage-like polyhedral shells consisting of 4- and 6-membered rings of alternately connected -B-N- are stable as stoichiometric closed networks in $(BN)_n$. Magic numbers are determined as $n = 12, 16, 28, 36 \ldots$. Pokropivny[23] also proposed 8-membered rings in addition to 4- and 6-. Experimentally $(BN)_n$ in polyhedral structure of ~1 nm was observed in electron microscope[24] and by mass spectrometry.[25]

Recent extensive calculations[21,26,27] reveal more possibilities of polyhedrons not only in the form of a hollow shell but also those placing atoms/molecules in the center or around the shell for increasing stability and/or functionality. To search such nanoparticles experimentally, the mass measurement should be extended to larger particles over 1 nm in condensed vapor method and analyze magic number distributions in detail. Concurrently, these samples should be synthesized and tired to extract stable ones in macroscopic quantity for the purpose of identification and precise analyses. Our recent investigation in CdSe (Ref. [28]) followed this approach and finds magic number of $(CdSe)_n$ with $n = 13$, 19, 33 and 34 in the mass analysis of both vapor and solution grown samples. It also finds $(CdSe)_{33}$ and $(CdSe)_{34}$ as stable nanoparticles preferentially grown in atomic precision as identified in sharp excitonic peak at 415 nm in the optical absorption spectrum in solution.

In this paper we present results of time-of-flight mass spectroscopy (TOF-MS) of heteroatomic nanoclusters with tens of atoms which form in the plasma plume produced in vacuum by laser ablation of powders for some of the $A_{II}B_{VI}$ compounds. Our experimental results for the mentioned size range demonstrate that nanoclusters with $n = 13$, 33 and 34 for $(CdSe)_n$, $(CdS)_n$, $(CdTe)_n$, $(ZnSe)_n$, $(ZnS)_n$, $(ZnTe)_n$ possess unique stability. These nanoclusters are the first reliably identified ultra-stable stoichiometric II–VI compound nanoclusters. Besides that it was found that $(CdSe)_{48}$ is a next stable nanoparticle preferentially grown in solution. Thus, presented experimental data demonstrate that in the transition range of sizes from atoms to bulk fragments, there is exceptional stability for clusters with stoichiometric Cd:Se ratio as 1:1 and numbers of CdSe molecules 13, 33, 34, and 48. A possible explanation of their elevated stability is specific structure different from the bulk one.

Such molecular particles extractable from solution may be quite stable against coalescence to each other or reaction with others in contact and called "ultra-stable" compared with magic number particles detected in vacuum that are relatively stable under isolated environments. Ultra-stable nanoparticles are particularly suited as functional blocks for assembling into a variety of nanostructures.

2. SAMPLE PREPARATION AND MEASUREMENT DETAILS

Bulk samples used in our measurement were 99.99% pure powders of crystalline CdSe from Wako Pure Chemical Industries, Ltd., CdS, CdTe, ZnS, ZnTe and ZnSe–from Sigma-Aldrich, Co. A small amount of powder was pestled well in an agate mortar and then mixed with 0.5 ml of hexane. A portion of 1 μl was pipetted on a stainless steel target plate. After dried quickly, the plate with the sample was transferred to the mass spectrometer.

In addition, nanoparticles of CdSe were prepared in reverse micelles using decylamine as surfactant in toluene as described in Ref. [28]. Optical absorbance were measured on colloidal toluene solution of CdSe nanoparticles in 10 mm quartz cuvette with a Hitachi U-2000 spectrophotometer at room temperature.

All time-of-flight mass measurements were carried out using a Bruker Reflex III-T mass spectrometer equipped with a nitrogen laser of 337.1 nm wavelength, 0.5 mJ energy, 4 ns pulse width and 1 Hz repetition rate. Mass spectra were obtained for positively charged ions in linear mode without injecting cooling gas to the vaporizing source. Spectra for negative ions were similar but in low signal to noise ratios. Each spectrum is recorded by accumulating a total of about 500 laser shots on different points on the target source.

3. RESULTS AND DISCUSSION

3.1. Mass Spectra on Bulk Powders of $A_{II}B_{VI}$ Compounds

Figure 1(a) displays the time-of-flight mass spectrum of nanoparticles produced by laser ablation on powder of bulk wurtzite CdSe. It represents a typical distribution of high intensities in low mass region below 2,000 a.m.u. (atomic mass unit) followed by a diminishing tail toward high mass because smaller mass particles are produced or survived as stable species with much higher probabilities than larger ones in a violent vaporizing process.[29] Dominant peaks found are stoichiometric $(CdSe)_n$ spaced by 191.4 a.m.u. (=mass of Cd + Se) with prominent ones at $n = 13$, 33, 34, and less prominent at $n = 19$ that exhibit intensities notably higher than their immediate neighbors. These prominent peaks, recognized by magic numbers, may correspond to a set of particularly stable chemical species realized in their specific structure just at these numbers of n. Since our measurements use no cooling gas during laser ablation, abundantly observed high mass particles must be extremely stable ones. The mass numbers, however, are quite unexpected from any set or series known

RESEARCH ARTICLE

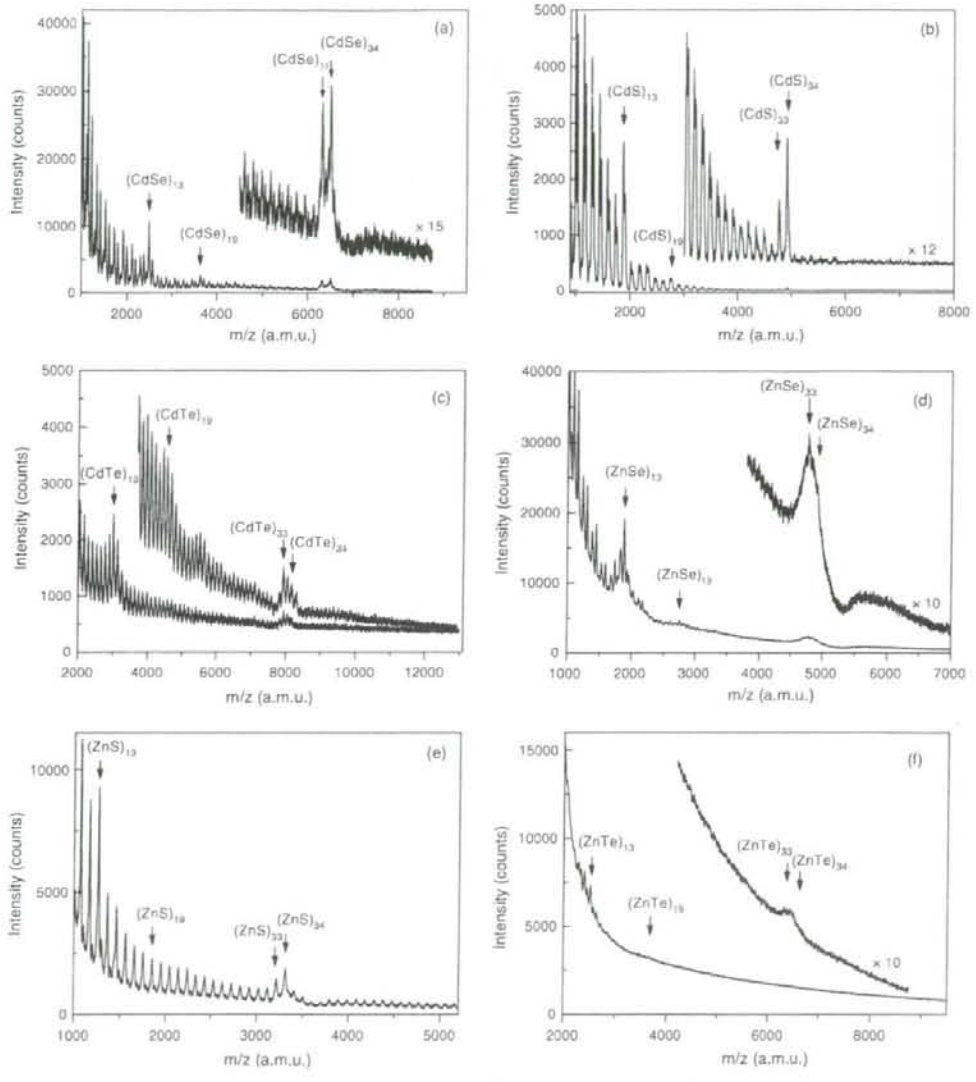

Fig. 1. Mass-spectra of $A_{II}B_{VI}$ nanoparticles formed in laser ablation of crystalline powders of CdSe (a), CdS (b), CdTe (c), ZnSe (d), ZnS (e), ZnTe (f). For some compounds the spectra near $n = 33$, 34 are expanded in intensity scale.

in the past. The peculiar feature lies after $n = 19$ that two consecutive number peaks appear sharply at $n = 33$ and 34 with distinctively high intensities of nearly equal magnitudes and contrastingly, the rest of all neighboring peaks are diminishingly small evenly. This behavior is hard to realize in bulk fragment models based on zinc-blende or wurtzite crystal in $A_{II}B_{VI}$ compounds.[1,18] Because of an open structure, the stability of fragment would not depend drastically on n, and cannot be equally so high particularly at two consecutive number particles and equally so low for all others in a wide range from their immediate neighbors.

The above spectral features are found common in other $A_{II}B_{VI}$ compounds, CdS, CdTe, ZnSe, ZnS and ZnTe, as shown in Figures 1(b)–(f), respectively. All show prominent peaks at $n = 33$ and 34, though details are different. Among them, CdSe exhibits the highest intensity ratio of

these two peaks to diminishingly weak neighbors in a wide mass range. This ratio is still high in CdS and ZnS with respect to higher masses but not so much for lower. In CdTe, ZnSe and ZnTe, neighbors on both sides exhibit rather high intensities. In ZnSe and ZnTe, each mass peak becomes broader and overlapping partly because higher laser intensity is necessary to obtain these spectra. Considerable fragmentation is evident especially towards low masses. At the highest laser intensity, a group of peaks appear near $n = 23$ in the measurement tuned for high mass region, as seen in the upper curve of Figure 1(c) on CdTe.

The intensity ratio of stoichiometric peaks to non-stoichiometric is also distinctively different. It is quite high in CdSe, CdS and, ZnS, but nearly unity in CdTe. Non-stoichiometric peaks are almost absent in ZnS in the entire mass range, and also in CdS but in $n > 30$ only. Double peaks in $n < 30$ correspond to $(CdS)_n$ and non-stoichiometric Cd_nS_{n+1}. The intensity of $Cd_{n+1}S_n$ on the other hand is extremely week. In Figure 1(c) on CdTe, Cd_nTe_{n+1} and $Cd_{n+1}Te_n$ would overlap to each other because atomic masses of Cd and Te are comparable, and these peaks cannot be distinguished in the spectrum. All these detailed differences found in Figure 1 may be used to study the stability and structure of $(A_{II}B_{VI})_n$.

In ZnS, previous mass analyses[1, 18] show strong stoichiometric peaks including $n = 13$ and 34 but neighboring and non-stoichiometric peaks are also relatively strong. This spectral profile is different from Figure 1(e) probably because of the difference in vaporization conditions. Our measurement uses no cooling gas and detects stable ones more selectively.

3.2. $(CdSe)_{33\ 34\ 48}$ Nanoclusters Prepared in Solution

Figure 2(a) displays mass spectra of CdSe nanoparticles prepared in solution. Curve 1 shows peaks at $n = 33$ and 34 which are much more pronounced relative to neighboring peaks than in Figure 1(a) of the bulk powder. These two peaks are also sharper than in Figure 1(a) and their widths are explained by isotope distributions of natural Cd and Se. Furthermore, low mass peaks near $n = 13$ are much weaker compared with $n = 33$ and $n = 34$ than in Figure 1(a). These results indicate that the sample dried on the target plate contains $(CdSe)_{33}$ and $(CdSe)_{34}$ as the main species selectively grown in solution because of their extremely high stabilities among others. The incident laser energy in this measurement was less than half of the bulk in Figure 1(a). These ultra-stable particles, therefore, are gently evaporated from the target plate as original chemical species rather than formed and ejected under a violent laser ablation process observed in the bulk powder measurement. The absence of peaks from surfactant and solvent implies that they are not firmly attached to these nanoparticles. Raising laser energy tends to increase neighboring

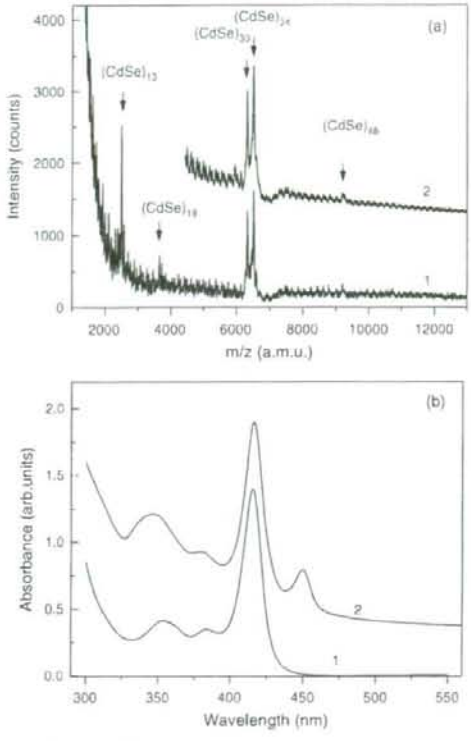

Fig. 2. Time-of-flight mass spectra (a) and absorption spectra (b) of CdSe nanoparticles grown by wet chemistry method in toluene for 1 day (curves 1) and for 13 days (curves 2).

peaks below $n = 33$ that accounted for by fragmentations of particles with $n = 33$ and 34 under laser excitation.

Curve 2 in Figure 2(a) displays a spectrum on the solution grown CdSe nanoparticles that are kept for 13 days at room temperature in toluene solution after synthesis. It shows $(CdSe)_{48}$ that is more pronounced than in Curve 1. This result indicates that $(CdSe)_{48}$ is also stable and selectively grown in solution during the aging period. Nanoparticles are surrounded by surfactants in reverse micelles that prevent from fast growth.

Curves 1 and 2 in Figure 2(b) correspond to optical absorption spectra of our samples in solution corresponding to Curves 1 and 2 in Figure 2(a), respectively. Curve 1 shows the main excitonic peak at 415 nm together with 382 nm and 352 nm. These peaks always show the same intensity ratios in our samples and belong to the same nanoparticle. Optical properties in CdSe nanoparticles of diameters larger than 1 nm have been studied extensively in Refs. [2, 3, 11, 30], and the main peak is found to blue shift as the diameter gets smaller by quantum confinement of electronic states in CdSe from 720 nm of the bulk

RESEARCH ARTICLE

absorption edge. From the peak at 415 nm in Figure 2, the diameter is estimated as ~1.5 nm, in agreement with our AFM measurement on dried sample.[28] Based on the main peak position, diameter and mass analysis, the main species in solution are attributed to $(CdSe)_{33}$ and $(CdSe)_{34}$. If the bulk density is assumed, simple calculation shows that 1.5 nm of crystalline CdSe sphere contains about 30 Cd-Se pairs.

Curve 2 in Figure 2(b) shows the 415 nm peak slightly broader with a tail structure developed towards longer wavelength compared with Curve 1. In Figure 2(a) on the other hand, Curve 2 shows mass peaks above $n = 34$ slightly increased especially at $n = 48$ compared with Curve 1. These results indicate the growth of nanoparticles larger than $(CdSe)_{34}$ during the 13 day aging, and $(CdSe)_{48}$ may be another stable nanoparticle preferentially grown in solution.

Curve 1 in Figure 2(b) is quite similar to those reported previously on very small CdSe nanoparticles grown in different solution methods.[2, 11, 30–34] All incidentally show the sharp and strong main peak near 415 nm with almost identical overall spectral profiles, and the diameter is estimated as ~1.2 nm (Ref. [2]) and ~1.7 nm.[11] The peak width is in remarkable contrast to much broader ones typically observed above 450 nm on samples of larger diameters.[2, 3, 11] Our samples prepared at 80 °C and above exhibit a broad main peak centered at 480 nm and above.[28] These nanoparticles essentially have bulk crystalline structures and their stabilities do not depend sharply on diameter as expected from the open structure of bulk fragments. This is a main reason that they grow in wide diameter distributions in solution showing a broad peak. Samples in Figure 2 prepared at room temperature, on the other hand, show the same sharp and strong peak at 415 nm with nearly identical profile under a wide reaction conditions.

If a particle is made smaller and smaller down to 1 nm, the number of constituent atoms becomes less than a hundred and begins to play a decisive role in size and shape dependent stabilities that only those particles in a set of particular numbers become stable and grow preferentially in solution, resulting in discrete single-size distributions. Extremely sharp 415 nm peak and its observations in different methods of preparation[2, 11, 30–33] show the presence of this sharp selective process.

It looks a bit unusual that two ultra-stable clusters with $n = 33$ and $n = 34$ are so close. One can suppose that they are pieces of a parent cluster $(CdSe)_{67}$ broken in the mass-spectrometer. We paid special attention to look for it and also for clusters like $n = 46$, $n = 47$, $n = 80$, etc. But nothing was found in the large mass range except the weak peak of the $n = 48$ cluster mentioned above. Probably only these clusters have specific ultra-stable arrangements of atoms that are different from the bulk structure. Larger species have crystal-like zinc-blende or wurtzite structures with no precise stoichiometry and a size distribution of 5–15% as reported in Ref. [2]. Possible structures of stoichiometric ultra-stable clusters with $n \leq 48$ will be discussed below.

Mass spectra confirmed another unusual result obtained earlier in sample characterization. Energy disperse X-ray analysis gave the Cd:Se ratio as 1:1 within the accuracy of the instrument. It's hard to expect precise stoichiometry for such small clusters when even usually the crystalline semiconductor clusters demonstrate a deviation from stoichiometry when their sizes decrease.

3.3. Mass Spectra on Some $A_{III}B_{V}$ Compounds and Related Materials

The importance of stoichiometry in the stability of $A_{II}B_{VI}$ compounds is indicated in comparison with mass spectra of $A_{III}B_{V}$ (A_{III} = Ga, In; B_{V} = N, P, Sb, As) shown in Figures 3(a) on GaAs and 3(b) on InSb measured similarly to those in Figure 1. In both 3(a and b), the spectra show strong mass peaks that are only in the low mass region below 2,000 a.m.u. and far from 1:1 stoichiometry of A_{III} to B_{V} with no simple rule. In addition, no prominent peak appears near $(A_{III}B_{V})_{14}$, indicating no particularly stable nanoparticles in this mass range. Similar results are found in GaP and GaN. These spectra indicate that nanoparticles of $A_{III}B_{V}$ have stable structures quite different from $A_{II}B_{VI}$. Apparently, the stoichiometry is not the major factor governing the stability, in sharp contrast to $A_{I}B_{VII}$ of alkali-halide which is shown by previous mass spectroscopic analyses to be stable in 1:1 composition as small cuboids of the face-centered-cubic lattice.[1, 34] In these stable cuboids of ionic crystal, the charge is well balanced in atoms of both polarities connected alternately to each other in every direction along the lattice in a symmetric arrangement.

Such balance is difficult to achieve in the fragment of bulk $A_{III}B_{V}$ without some sort of reformation of the tetrahedral coordination. The directional and strong covalent bonds make this reformation energetically unfavorable at any number of constituent atoms and may leave the stability of bulk fragment rather size-insensitive, as seen in flat high mass distributions in Figures 3(a and b).

Because of the increasing ionicity and decreasing covalency from $A_{III}B_{V}$, nanoparticles of $A_{II}B_{VI}$ may be stabilized favorably by balancing the charge tightly in 1:1 stoichiometry with alternating network of A_{II} and B_{VI} in high symmetry reformed from the tetrahedral lattice fragment. Such energetically favorable rearrangements of atoms can be realized in small particles only at limited n's, as expected in our measurements.

Time-of-flight mass spectra with laser excitation depend so sensitively on the experimental condition of target vaporization and nanoparticle extraction from the vapor that measurements on different materials obtained with the same instrument are quite reliable and useful for detailed spectral analysis and comparison to find stable and useful

RESEARCH ARTICLE

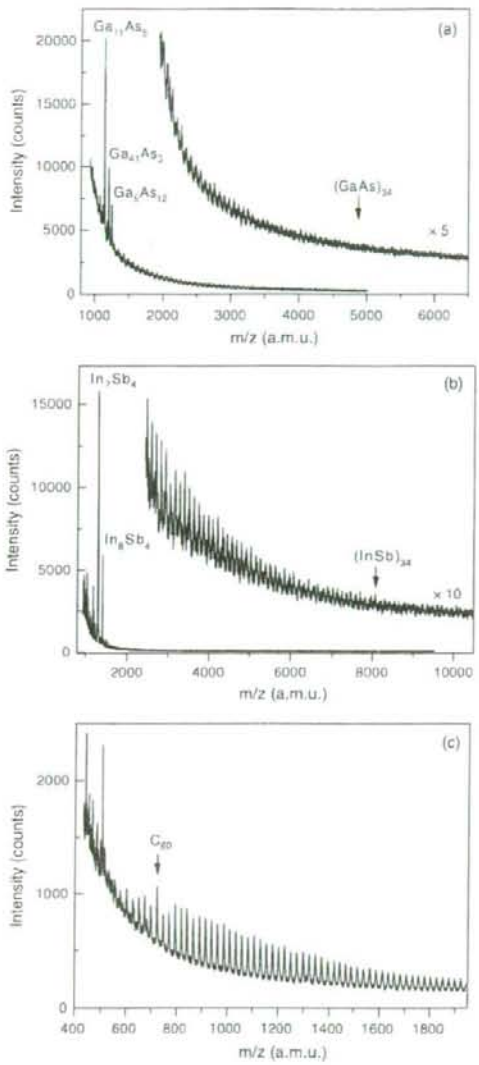

Fig. 3. Mass-spectra of $A_{II}B_{VI}$ nanoparticles formed in laser ablation of crystalline powders of GaAs (a), InSb (b) and graphite (c).

nanoparticles. Figure 3(c) displays the result on graphite powder to show how stable $(A_{II}B_{VI})_{13}$, $(A_{II}B_{VI})_{33}$ and $(A_{II}B_{VI})_{34}$ are compared with their neighboring masses. It exhibits strong peak at C_{60} together with neighboring C_n of even n in comparable magnitudes in the tail of intense low mass peaks. The C_{60} peak is not particularly strong since no cooling gas is introduced on the vapor of C_n. The Figure 3(c) is in contrast with the prominent peaks of $(A_{II}B_{VI})_{33}$ and $(A_{II}B_{VI})_{34}$ also without cooling gas that show their extremely selective stabilities. Historically, the spectrum in laser ablation on graphite provided a decisive experimental fact to model the atomic arrangement of C_{60} (Ref. [35]) which is entirely different from bulk diamond or graphite. The experimental identification, however, had awaited its chemical synthesis five years later in macroscopic quantity[36] for the structural analysis in atomic precision. Our systematic measurement shows extremely selective stabilities of $(A_{II}B_{VI})_n$ and opens up the possibility to find more stable molecular-like particles extended from elemental carbon only to the vast variety of compound systems.

4. STRUCTURE OF ULTRA-STABLE $(A_{II}B_{VI})_n$ NANOCLUSTERS

The observation of ultra-stable clusters consisting of ten to hundreds of atoms assumes their specific structure. To date, published theoretical approaches applied to clusters of CdSe and related compounds in Refs. [1, 6, 37–39] considered them as fragments of bulk wurtzite or zinc-blende lattice with relaxed surface atoms but their calculations did not show agreement in ultra-stable compositions.

From the comparison of the mass spectra we can conclude that $n = 13$, 33 and 34 are magic numbers for ligand-free clusters for all the II–VI compounds studied here. Also, from our experiments with colloid solution we can conclude that $(CdSe)_{13}$, $(CdSe)_{33}$, $(CdSe)_{34}$ and $(CdSe)_{48}$ are ultra-stable clusters with ligand passivated surface. These numbers, especially for two consecutive 33 and 34 are difficult to explain consistently by open structures of compact crystalline fragments. The model by Martin[1] based on zinc-blende predicts $n = 13, 34, 70, 125, \ldots$, but not for 33 particularly. The basket model by Burnin[18] is presented only for $n = 13$.

The cage model by Seifert[22] in $(BN)_n$, on the other hand, has more possibility of explaining the stability.[28] The cage has a space at the center that can be filled by more atoms without affecting much the polyhedral morphology of closed structure. In more ionic compounds like $A_{II}B_{VI}$ compared with BN, polyhedrons are more stable by distributing atoms of both polarities alternately in the entire volume than only around the surface, especially in larger ones. Tetrahedral sp^3 bondings of these compounds are also favorable of three-dimensional distribution than sp^2 of two-dimensional. The model of $(BN)_n$ predicts magic numbers corresponding to closed empty cages as $n = 12, 16, 28, 36, \ldots$.

For binary compounds of normally 4-coordinated atoms, the probable building block is the 6-membered ring. And to have closed structure instead of plain sheet, some rings must be smaller ones–4-membered (5-membered rings observed in C_{60} and C_{70} are impossible for binary compounds with some ionicity). But we failed to construct symmetrical cage-like structure of $33 + 33$ or $34 + 34$

RESEARCH ARTICLE

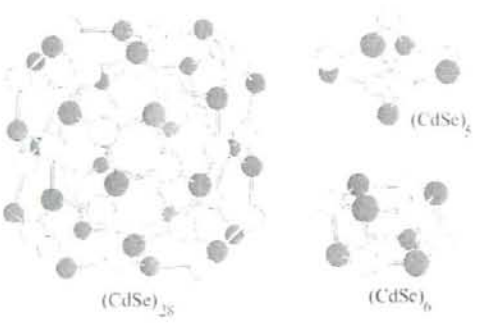

Fig. 4. Proposed structures for $(CdSe)_{34}$ and $(CdSe)_{34}$ clusters—empty $(CdSe)_{28}$ cage and internal patterns $(CdSe)_6$ and $(CdSe)_6$.

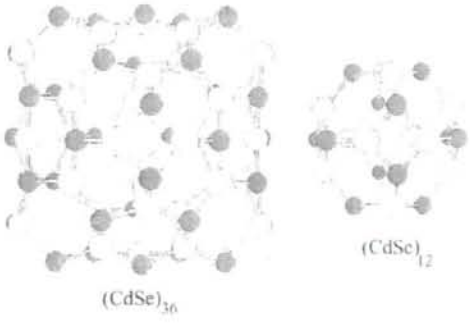

Fig. 5. Proposed structure for $(CdSe)_{48}$ cluster—outer cage $(CdSe)_{36}$ and internal cage $(CdSe)_{12}$.

atoms under these rules. The nearest high symmetry ball-like structure consists of 28 + 28 atoms and has 6 4-membered rings (Fig. 4). This contradiction can be resolved if we put inside another small pattern consisting of 5 + 5 or 6 + 6 atoms and composed also of 6-membered rings (Fig. 4). Its size matches well with the outer shell and the angular Cd atoms can form 3D bonds with the shell Se atoms (fourfold coordination). Saturation of the Cd atoms bonds partly decreases the dangling bonds number and reconstruction of the surface occurs (because more than 80% of atoms in particles are surface atoms). Stabilization of the clusters occurs by filling them inside with an additional network that acts as a core that is strongly interconnected to the outer cage. If we operate only with the experimental result from the mass spectrometry of the stoichiometric composition $(A_{II}B_{VI})_{34}$, then for the proposed cage-like structure with core $(CdSe)_6$ the number of dangling bonds is 56 (coordination number $N = 3.18$), while for the wurtzite bulk fragment proposed in Ref. [1] there are 62 dangling bonds and the coordination number $N = 3.09$ is lower. Typically, computer optimized cage-like structures have binding energies a few eV higher than bulk fragments.[28, 40] Saturation of bonds also causes the minimum of chemical reactivity. Maybe for the binary II–VI compounds it is essential to have a certain pattern inside the shell to keep it from collapse, and two possible internal patterns explain the two lines in the mass spectrum while in general the particles are very similar. The observation of stoichiometric nanoparticles is a strong indication that the charge balance is an important factor in determining the stability, and the detailed spectral differences in Figures 1(a) to (f) may be attributed partly to states of ionicity in these $A_{II}B_{VI}$ compounds. More experimental investigation is necessary for further analyses.

For the $(CdSe)_{28}$ cluster, a similar nested cage structure can be suggested. The nearest binary fullerene shell is at $n = 36$. Thus it has to incorporate $n = 12$ molecules. But that is exactly the composition of smallest shell (Fig. 5). Simple estimates of the difference of their diameters give a value which is very close to the Cd—Se bond length. It means that the $n = 12$ cage fits well into the $n = 36$ cage and that some atoms can form bonds between cages. Extensive first principle calculations[28] confirmed the high binding energies of the suggested structures of CdSe ultra-stable clusters.

5. CONCLUDING REMARKS

Time-of-flight mass analysis reveals that small particles of binary $A_{II}B_{VI}$ compounds are extremely stable in the stoichiometric form of $(A_{II}B_{VI})_n$ with $n = 13$, 19, 33 and 34, as observed abundantly over weak neighbors in laser ablation on bulk powders of CdSe, CdS, CdTe, ZnS, ZnSe. The remarkable stability of $(A_{II}B_{VI})_{33}$ and $(A_{II}B_{VI})_{34}$ is well demonstrated by the fact that massive particles of ~1 nm in diameter are produced selectively at only two specific mass numbers without intentionally cooling the vapor ejected in a violent ablation process in vacuum. This result has not been predicted in the past but is found common to all $A_{II}B_{VI}$ compounds measured in our simple experiment. These numbers and stoichiometry are particular to $A_{II}B_{VI}$ compounds and not to $A_{III}B_V$. The observed mass range lies in the gap between those of samples typically produced in vacuum and in solution, corresponding to the intermediate region between molecule and solid.

In cadmium selenide, $(CdSe)_{13}$, $(CdSe)_{34}$ and $(CdSe)_{68}$ are even found to grow preferentially in solution at room temperature by suppressing the formation of smaller and larger neighbors. This sharp selective stability enables us to obtain truly single-size stoichiometric nanoparticles in macroscopic quantity at precision expressed by the number of atoms instead of diameter.

Our experimental results show the presence of such ultra-stable nanoparticles of compounds having three-dimensional chemical bonds, like sp^3. These molecular nanoparticles are expected to have structures and properties uniquely specified by the number of constituent atoms. This specific structure must be different from the close

RESEARCH ARTICLE

packed arrangements of atoms in fragments of bulk crystals. One suggestion for structure of these clusters is a highly symmetric cage of binary fullerenes with a few additional atoms inside providing the stability of such heteroatomic compositions. These atomically well-defined materials not realized in the bulk serve as extremely useful functional units for basic studies in nanometer sciences and for a variety of device applications.

Acknowledgments: Authors would like to thank Dr. M. Kobayashi for helpful discussions and technical collaboration during mass-spectroscopy measurements. This work was supported in part by Grant-in-aid from the Ministry of Education in Japan.

References and Notes

1. T. P. Martin, *Phys. Reports* 273, 199 (**1996**); T. P. Martin, T. Hergmann, H. Gohlich, and T. Lamge, *J. Phys. Chem.* 95, 6421 (**1991**).
2. C. B. Murray, D. J. Norris, and M. G. Bawendi, *J. Am. Chem. Soc.* 115, 8706 (**1993**).
3. X. Peng, L. Manna, W. Yang, J. Wickham, E. Scher, A. Kadavanich, and A. P. Alivisatos, *Nature* 404, 59 (**2000**).
4. J. H. Adair, T. Li, T. Kido, K. Havey, J. Moon, J. Mecholsky, A. Morrone, D. R. Talham, M. H. Ludwig, and L. Wang, *Mater. Sci. Eng.* R23, 139 (**1998**).
5. M. C. Troparevsky and J. R. Chelikowsky, *J. Chem. Phys.* 114, 943 (**2001**).
6. P. Deglmann, R. Ahlrichs, and K. Tsereteli, *J. Chem. Phys.* 116, 1585 (**2002**).
7. T. Sugimoto, G. E. Dirige, and A. Muramatsu, *J. Coll. Interf. Sci.* 182, 444 (**1996**).
8. N. Pinna, K. Weiss, J. Urban, and M.-P. Pileni, *Adv. Mater.* 13, 261 (**2001**).
9. M. Chatterjee and A. Patra, *J. Am. Ceram. Soc.* 84, 1439 (**2001**).
10. H.-L. Li, Y.-C. Zhu, S.-G. Chen, O. Palchik, J.-P. Xiong, Y. Koltypin, Y. Gofer, and A. Gedanken, *J. Sol. State Chem.* 172, 102 (**2003**).
11. V. Ptatschek, C. Schmidt, M. Lerch, G. Muller, L. Spanhel, A. Emmerling, J. Fricke, A. H. Foitzik, and E. Langer, *Ber. Bunsenges. Phys. Chem.* 102, 85 (**1998**).
12. S. Gorer and G. Hodes, *J. Chem. Phys.* 98, 5338 (**1994**).
13. N. Gaponik, D. V. Talapin, A. L. Rogach, K. Hoppe, E. V. Shevchenko, A. Kornowski, A. Eychmuller, and H. Weller, *J. Phys. Chem. B* 106, 7177 (**2002**).
14. A. L. Rogach, N. A. Kotov, D. S. Koktysh, A. S. Susha, and F. Caruso, *Colloids and Surfaces A: Physicochemical and Engineering Aspects* 202, 135 (**2002**).
15. D. V. Talapin, A. L. Rogach, I. Mekis, S. Haubold, A. Kornowski, M. Haase, and H. Weller, *Colloids and Surfaces A: Physicochemical and Engineering Aspects* 202, 145 (**2002**).
16. Y.-W. Cao and U. Banin, *Angew. Chem. Int. Ed.* 38, 3692 (**1999**).
17. K. Koga, T. Ikeshoji, and K.-C. Sugawara, *Phys. Rev. Lett.* 92, 115507-1 (**2004**).
18. A. Rumin and J. J. BelBruno, *Chem. Phys. Lett.* 362, 341 (**2002**).
19. A. Nakajima, N. Zhang, H. Kawamata, T. Hayase, K. Nakao, and K. Kaya, *Chem. Phys. Lett.* 241, 295 (**1995**).
20. M. Alberti, O. Sedo, and J. Havel, *Polyhedron* 22, 2601 (**2003**).
21. Q. Sun, Q. Wang, T. M. Briere, V. Kumar, and Y. Kawazoe, *Phys. Rev. B* 65, 235417-1 (**2002**).
22. G. Seifert, P. W. Fowler, D. Mitchell, D. Porezag, and Th. Frauenheim, *Chem. Phys. Lett.* 268, 352 (**1997**).
23. V. V. Pokropivny, V. V. Skorokhod, G. S. Oleinik, A. V. Kurdyumov, T. S. Bartnitskaya, A. V. Pokropivny, A. G. Sisonyuk, and D. M. Sheichenko, *J. Solid State Chem.* 154, 214 (**2000**).
24. O. Stephan, Y. Bando, A. Loiseau, F. Willamie, N. Shramchenko, T. Tamiya, and T. Sato, *Appl. Phys. A* 67, 107 (**1998**).
25. T. Oku, A. Nishiwaki, I. Narita, and M. Gonda, *Chem. Phys. Lett.* 380, 620 (**2003**).
26. Q. Sun, Q. Wang, P. Jena, B. K. Rao, and Y. Kawazoe, *Phys. Rev. Lett.* 90, 135503-1 (**2003**).
27. G. Belomoin, J. Therrien, A. Smith, S. Rao, R. Twesten, S. Chaieb, M. H. Nayfeh, L. Wagner, and L. Mitas, *Appl. Phys. Lett.* 80, 841 (**2002**).
28. A. Kasuya, R. Sivamohan, Yu. Barnakov, I. Dmitruk, T. Nirasawa, V. Romanyuk, V. Kumar, S. Mamykin, K. Tohji, B. Jeyadevan, K. Shinoda, T. Kudo, O. Terasaki, Zh. Liu, R. Belosludov, V. Sundararajan, and Y. Kawazoe, *Nat. Mater.* 3, 99 (**2004**).
29. Y.-M. Koo, Y.-K. Choi, K.-H. Lee, and K.-W. Jung, *Bull. Korean Chem. Soc.* 23, 309 (**2002**).
30. C. Landes and M. A. El-Sayed, *J. Phys. Chem. A* 106, 7621 (**2002**).
31. M. V. Artemyev, A. I. Bibik, L. I. Gurinovich, S. V. Gaponenko, and U. Woggon, *Phys. Rev. B* 60, 1504 (**1999**).
32. H. Wang, A. Tashiro, H. Nakamura, M. Uehara, M. Miyazki, T. Watrai, and H. Maeda, *J. Mater. Res.* 19, 3157 (**2004**).
33. J. H. Yoon, W. S. Chae, S. J. Im, and Y. R. Kim, *Mater. Lett.* 59, 1430 (**2005**).
34. A. W. Castleman, Jr., and K. H. Bowen, Jr., *J. Phys. Chem.* 100, 12911 (**1996**).
35. H. W. Kroto, J. R. Heath, S. C. O'Brien, R. F. Curl, and R. E. Smalley, *Nature* 318, 162 (**1985**).
36. W. Kraetschmer, L. D. Lamb, K. Fostiropoulos, and D. R. Huffman, *Nature* 347, 27 (**1990**).
37. J. O. Joswig, M. Springborg, and G. Seifert, *J. Phys. Chem. B* 104, 2617 (**2000**).
38. K. Leung and K. B. Whaley, *J. Chem. Phys.* 110, 11012 (**1999**).
39. K. Eichkorn and R. Ahlrichs, *Chem. Phys. Lett.* 288, 235 (**1998**).
40. U. Rothlisberger, W. Andreoni, and M. Parrinello, *Phys. Rev. Lett.* 72, 665 (**1994**).

Received: 3 March 2008. Accepted: 24 March 2008.

RESEARCH ARTICLE

Takashi Kandori
Graduate School of Engineering,
Tohoku University,
6-6 Aramaki-Aoba,
Aoba-ku, Sendai 980-8579, Japan

Toshiyuki Hayase[1]
Institute of Fluid Science,
Tohoku University,
2-1-1 Katahira,
Aoba-ku, Sendai 980-8577, Japan

Kousuke Inoue

Kenichi Funamoto

Takanori Takeno

Institute for International Advanced
Interdisciplinary Research,
International Advanced Research and
Education Organization,
Tohoku University,
6-3 Aramaki-Aoba,
Aoba-ku, Sendai 980-8578, Japan

Makoto Ohta
Institute of Fluid Science,
Tohoku University,
2-1-1 Katahira,
Aoba-ku, Sendai 980-8577, Japan

Motohiro Takeda
Graduate School of Medicine,
Tohoku University,
2-1 Seiryo-machi,
Aoba-ku, Sendai 980-8574, Japan

Atsushi Shirai
Institute of Fluid Science,
Tohoku University,
2-1-1 Katahira,
Aoba-ku, Sendai 980-8577, Japan

Frictional Characteristics of Erythrocytes on Coated Glass Plates Subject to Inclined Centrifugal Forces

In recent years a diamond-like carbon (DLC) film and a 2-methacryloyloxyethyl phosphorylcholine (MPC) polymer have attracted attention as coating materials for implantable artificial organs or devices. When these materials are coated on vascular devices, compatibility to blood is an important problem. The present paper focuses on friction characteristics of erythrocytes to these coating materials in a medium. With an inclined centrifuge microscope developed by the authors, observation was made for erythrocytes moving on flat glass plates with and without coating in a medium of plasma or saline under the effect of inclined centrifugal force. Friction characteristics of erythrocytes with respect to these coating materials were then measured and compared to each other to characterize DLC and MPC as coating materials. The friction characteristics of erythrocytes in plasma using the DLC-coated and noncoated glass plates are similar, changing approximately proportional to the 0.5th power of the cell velocity. The cells stick to these plates in saline as well, implying the influence of plasma protein. The results using the MPC-coated plate in plasma are similar to those of the other plates for large cell velocities, but deviate from the other results with decreased cell velocity. The results change nearly proportional to the 0.75th power of the cell velocity in the range of small velocities. The results for the MPC-coated plate in saline are similar to that in plasma but somewhat smaller, implying that the friction characteristics for the MPC-coated plate are essentially independent of plasma protein. [DOI: 10.1115/1.2948420]

Keywords: erythrocytes, friction characteristics, inclined centrifuge microscope, DLC, MPC polymer, glass plate, plasma

1 Introduction

Blood flow in microcirculation plays an important role in supplying tissues with nutrients and removing metastases. Extensive physiological research has been carried out to examine blood flow in microcirculation focusing on the complex interaction between blood cells, plasma proteins, and glycocalyx in the endothelial surface layer [1,2]. Numerical analysis has been performed for cell motion in a blood capillary considering the interaction between the cell and the endothelial surface layer [3], but there have been little experimental measurement data of friction characteristics to date. It is critically important to develop a method to measure this friction force acting on the blood cells moving along the vessel surface.

The centrifuge microscope enables us to observe cells under centrifugal force [4], and, to date, several different types of centrifuge microscope have been developed [5]. These devices have been used to investigate various cell characteristics, for example, the mechanical properties of the Echinoderm egg [6], the motive force of paramecia [7], and the force-velocity relation of muscle fibers [8]. However, all existing centrifuge microscopes are designed such that the direction of cell deformation or movement and the direction of centrifugal force are identical, and the magnitude of the centrifugal force is the only parameter to be specified (see Fig. 1(*a*)). The present study uses the inclined centrifuge microscope [9], which enables us to observe cells on an inclined plane while specifying the tangential and normal force components of the centrifugal force independently (Fig. 1(*b*)). In order to gain a fundamental understanding of the blood cell interaction

[1]Corresponding author.

Contributed by the Bioengineering Division of ASME for publication in the Journal of Biomechanical Engineering. Manuscript received August 23, 2007; final manuscript received March 11, 2008; published online July 14, 2008. Review conducted by Fumihiko Kajiya.

 Copyright © 2008 by ASME

Downloaded 14 Jul 2008 to 130.34.231.209. Redistribution subject to ASME license or copyright; see http://www.asme.org/terms/Terms_Use.cfm

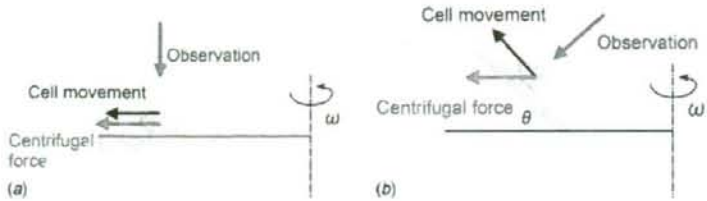

Fig. 1 Comparison between conventional and inclined centrifuge microscope: (*a*) conventional centrifuge microscope and (*b*) inclined centrifuge microscope

mentioned above, the present study investigated the friction characteristics of erythrocytes moving along material-coated glass plates in plasma or saline using the inclined centrifuge microscope.

In recent years materials for coating implantable artificial organs or devices have attracted attention. Among them this paper deals with diamond-like carbon (DLC) film [10] and 2-methacryloyloxyethyl phosphorylcholine (MPC) polymer [11]. DLC is one of the carbon based coatings with amorphous structure, which has properties similar to diamond. It has good resistance to corrosion and wear, low coefficient of friction, low partner aggressiveness, superflat smoothness, a thin film, and insulation properties. MPC was developed to create biomembrane structures artificially. It has a phosphorylcholine base that has a phospholipid polar group side chain and has a characteristic to restrain proteinaceous absorption.

When the DLC or MPC polymer is coated on vascular devices, compatibility to blood is an important problem. The present paper focuses on friction characteristics of erythrocytes to these coating materials in a medium. The inclined centrifuge microscope is used first to observe the motion of erythrocytes moving on flat glass plates with and without coating of DLC or MPC polymer in a medium of plasma or saline under the effect of centrifugal force at an angle with respect to the plate. Friction characteristics of erythrocytes to these materials are then measured and compared with each other to characterize DLC and MPC polymer as a coating material from the viewpoint of the friction property of erythrocytes.

2 Experimental Apparatus and Principle

2.1 Inclined Centrifuge Microscope. A schematic and specifications of the inclined centrifuge microscope system are shown in Fig. 2 and Table 1, respectively. In order to improve measurement performance, several components of the original equipment [9] have been replaced in the present system. A pair of inclined containers of inner dimension of $10 \times 8 \times 1$ mm^3 (width $\times$ length $\times$ height) is mounted on the rotor of the centrifuge (KUBOTA, Model 1120). One of the two containers is filled with a medium containing blood cells and the other container remains empty. The rotation speed of the rotor is measured using a digital tachometer (ONO SOKKI, TM-2110, error: 0.02%). A reference signal of rotation, which is generated by a laser diode (NEO ARK, LDP-6930C) and a detector (NEO ARK, RD-102), and is delayed through a pulse generator (Hewlett-Packard, HP81101A, 50 MHz) and a signal synthesizer (NF Circuit Design Block, WF1944), triggers an yttrium aluminum garnet (YAG) laser (KANOMAX, SPIV-30-20-ATT, 3 ns/pulse, 30 mJ/pulse) and a charge coupled device (CCD) camera (Ikegami, SKC-141, 15 fps, 145 megapixels). The exposure time of the CCD camera is fixed at 1/8000 s and the exposure timing is controlled to accurately synchronize with the rotation. The laser beam, which is guided through an optical fiber (NIKON, GFLG-5), illuminates the container for a very short interval of 3 ns during the exposure time of the CCD camera at the same angular position of the spinning rotor so that a still image of the plate can be observed. Erythrocytes moving on the plate are observed through a microscope (NIKON, CM-10) with objectives (Olympus, Cplan FI 10× and CF Plan EPI SLWD 50×), the light axis of which is adjusted normal to the plate at an angle of θ from the horizontal plane. The microscope was remodeled to change the optical axis 90 deg by mirroring at the connecting point of the objective lens. The images are sent to a PC and stored on its hard drive.

In each measurement, 100 sequential images with an interval of the smallest multiple of the rotation period larger than 1/15 s were obtained. Each image was digitized into 1392 $\times$ 1024 pixels with a 256-level monochrome gradation and a diameter of 0.65 μm/pixel for the 10× objective lens. Fluctuation of the images due to inevitable error in synchronization was removed by translating the images based on grid lines of 5 μm in width etched on the back of the plates. The image data were

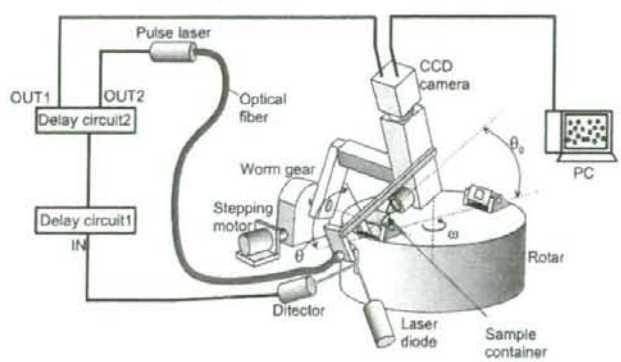

Fig. 2 Schematic of the inclined centrifuge microscope system

Downloaded 14 Jul 2008 to 130.34.231.209. Redistribution subject to ASME license or copyright; see http://www.asme.org/terms/Terms_Use.cfm

Table 1 Specifications of inclined centrifuge microscope

Angle of microscope	θ_0	0–50 deg
Angle of base plate	θ	40–90 deg
Angular frequency	ω	0–1257 rad/s
Magnification on 17 in monitor (10× and 50× objective lens)		×255, ×1275
Rotation radius	r_0	5.43×10^{-2} m
Rotation speed	N	0–12,000 rpm

processed by the PTV software program (Nexus, PIV EXPERT 2000) to obtain the velocity vectors of the erythrocytes. After the removal of background noise and smoothing, centers of gravity of all erythrocytes were obtained. The particle tracing velocimetry method was then applied in order to determine the velocity vectors of all the cells based on the distribution of cell centers at two time instants. The cell velocity is evaluated by the velocity component parallel to the tangential force since the rotational velocity component is strongly affected by the fluctuation in synchronization.

2.2 Principle of Friction Force Measurement. A schematic of the sample container is shown in Fig. 3. The plate is placed at the bottom of the container, which is inclined at an angle of θ from the horizontal plane (Fig. 3(*a*)). The container is filled with a medium (plasma or saline) in which erythrocytes have been dispersed. By applying rotation at an angular velocity ω, the cells move in a radial direction under the effect of centrifugal force F described as

$$F = (\rho_r - \rho_m)V_r r_0 \omega^2 \tag{1}$$

where ρ_r, ρ_m are the densities of the erythrocyte and the medium, respectively, V_r is the volume of the cell (Table 2), and r_0 is the rotation radius (Table 1). Note that we consider the case in which the effect of gravitation is negligible and the rotation radius is assumed to be constant. After the cells contact the plate, the centrifugal force on each cell is naturally divided into two components; the normal force F_N and the tangential force F_T (Fig. 3(*b*)) as

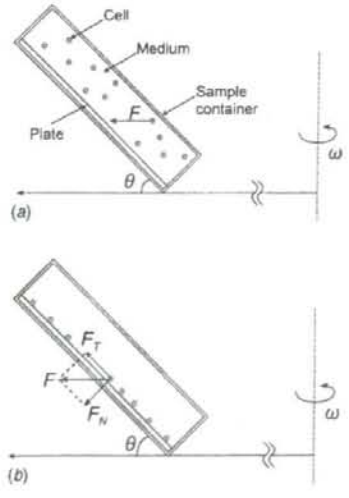

Fig. 3 Principle of friction force measurement in a rotating field: (*a*) initial state and (*b*) steady-state movement of erythrocytes

Table 2 Physical properties of specimen

Erythrocytes	
Diameter d_r	8.4×10^{-6} m
Height h_r	2.4×10^{-6} m
Volume V_r	8.7×10^{-17} m^3
Density ρ_r	1087 kg/m^3
Plasma	
Density ρ_p	1025 kg/m^3
Viscosity μ_p	1.2×10^{-3} Pa s
Saline	
Density ρ_s	998.2 kg/m^3
Viscosity μ_s	1.01×10^{-3} Pa s

$$F_N = F\sin\theta, \quad F_T = F\cos\theta \tag{2}$$

The normal force F_N balances the reaction from the plate, and the tangential force F_T accelerates the cell along the plate. When the cell velocity U reaches a steady value, the tangential force F_T is equal to the sum of the friction force F_T^* from the plate and the drag force f_D from the medium above the cell as

$$F_T = F_T^* + f_D \tag{3}$$

Precisely modeling the drag force for the shape of an actual erythrocyte is difficult. Since the Reynolds number based on the diameter and velocity of the cell and on the kinematic viscosity of the medium is less than 10^{-3} for the condition examined in the present study, we use the drag coefficient C_D of the Stokes equation for a sphere [12],

$$f_D = C_D(h_r d_r)\frac{1}{2}\rho U^2, \quad C_D = 24/R_e \tag{4}$$

where h_r and d_r denote the height and the diameter of the erythrocyte, respectively (Table 2).

As the force components F_N and F_T are specified arbitrarily by adjusting the angle of the container θ and the angular velocity ω, measuring the cell velocity U for a variety of force conditions gives the friction characteristics of the erythrocytes moving along the plate. A finite time is required before the cells attain a steady velocity with all forces in equilibrium.

By the assumption that the friction force is approximately described as the viscous friction of the uniform shear flow between the cell and the plate, we have the following equation:

$$F_T^* = \mu \cdot \dot{\gamma} \cdot \pi d_r^2/4 \tag{5}$$

where $\dot{\gamma}$ is the equivalent shear rate of the flow in a gap between the cell and the plate. The equivalent gap width h_g is given as

$$h_g = U/\dot{\gamma} \tag{6}$$

3 Materials and Methods

Human venous blood was sampled to a vacuum blood-collecting vessel (NIPRO NEO TUBE PET) from an informed healthy male volunteer of 24 years old. The blood anticoagulated by citric acid sodium (3.13%) was centrifuged (1000 g, 10 min) to separate plasma and erythrocytes. The plasma was centrifuged again in the same manner to purify it. A separate plasma and saline were then prepared as two mediums. Separated erythrocytes were distributed in the mediums at a volumetric concentration of 0.01%. The *p*H of the sample was 7.5 ± 0.1. The experiment was performed within 6 h after blood sampling and at a constant room temperature of 20 ± 1 °C. The physical properties of the materials are summarized in Table 2. The density of erythrocytes and that of the plasma are referred from our former study [9], whereas the other properties were obtained from literature [13].

Downloaded 14 Jul 2008 to 130.34.231.209. Redistribution subject to ASME license or copyright; see http://www.asme.org/terms/Terms_Use.cfm

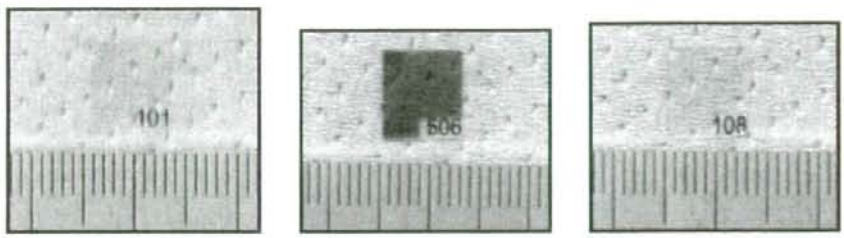

Fig. 4 Sample plates (small division=1 mm): (*a*) MPC-coated plate, (*b*) DLC-coated plate, and (*c*) noncoated plate

Pieces of cover glass made of synthetic quartz (Takahashi Giken Glass, 0.15 mm thickness) were used as the plates. Some of them were coated with DLC or MPC polymer. DLC coating was fabricated by chemical vapor deposition (CVD) technique. The deposition was performed for 20 min under the condition of 2.2×10^{-2} torr and −700 V of substrate self-bias voltage. A methane gas was used as a precursor gas. MPC polymer was coated on a different plate by putting the plate into PMB ethanol solution (0.2 wt %) and drying it naturally. The PMB ethanol is a mixture of non-water-soluble PMB30 and water-soluble PMB80 in a ratio of 9:1.

Figure 4 shows photographs of (*a*) a glass plate coated with MPC polymer (MPC-coated plate), (*b*) a glass plate coated with DLC (DLC-coated plate), and (*c*) a glass plate without coating (noncoated plate), respectively. The MPC-coated plates look the same as the noncoated plates. The DLC-coated plates are colored light brown but transparent.

Surface roughness of a noncoated plate and a DLC-coated plate was measured with an atomic force microscopy (AFM) (Veeco Enviroscope equipped with the NanoScope IV Controller). As shown in Fig. 5 the DLC-coated plate has larger roughness than the noncoated plate, but is still very smooth with roughness less than 10 nm. Since the probe used in the measurement was not applicable to soft surfaces, the surface roughness of MPC-coated plates was not measured.

4 Results

The motion of the erythrocytes on the three kinds of plates was first observed by using the 50× objective lens of the inclined centrifuge microscope. The friction characteristics were then measured by the 10× objective lens. In the experiment, tangential force component F_T was set between 2.5 pN and 40 pN while maintaining the normal force component F_N at 47 pN.

Figure 6 shows a snapshot of a motion picture in which erythrocytes (large circles) are moving upward in the figure on the MPC-coated plate in the medium of plasma under the effect of centrifugal force with a tangential force component F_T of 35 pN and a normal force component F_N of 47 pN. As mentioned above the tangential force component drives the cells to move on the plate and the normal force component pushes the cells on the plate. In the figure, the configurations of erythrocytes are clearly defined including a dark part in the center corresponding to a typical concave shape. The small dots in the figure are most likely aggregations of fibrinogen in plasma. Similar results were obtained for the noncoated plate and the DLC-coated plate under the same conditions.

For a relatively small tangential force of F_T=5 pN, some differences appear in the motion of erythrocytes between the plates. All the cells move on the MPC-coated plate, but some cells rest on the noncoated plate and more cells rest on the DLC-coated plate. The velocity of cells on the MPC-coated plate was larger than that of the others. The motion of moving cells on the DLC-coated plate fluctuated in a transverse direction in comparison with the other cases.

We then replaced plasma with saline as the medium. Figures 7(*a*) and 7(*b*) show the results for the MPC-coated and the DLC-coated plates, respectively, where F_T=30 pN and F_N=47 pN. Cells on the MPC-coated plate move smoothly but those on the DLC-coated plate stick to the plate stretching in the tangential force direction due to centrifugal force. The results of the noncoated plate were similar to that of the DLC-coated plate.

Next we measured the velocities of the cells to evaluate the friction characteristics of erythrocytes on the plates. In order to

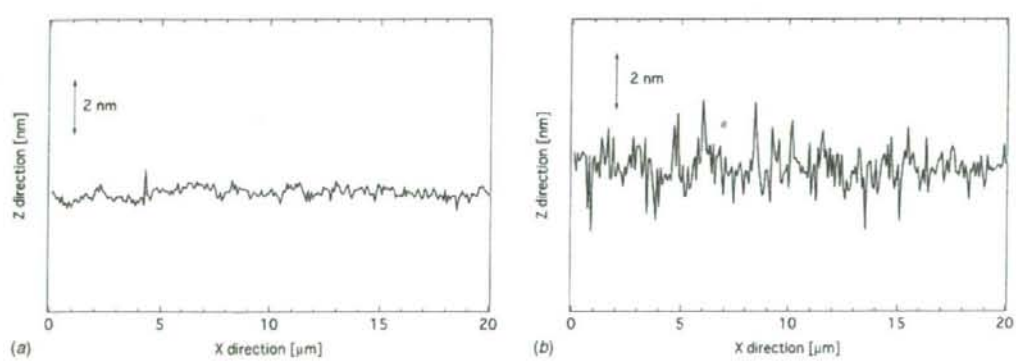

Fig. 5 Roughness of sample plates measured by AFM: (*a*) noncoated plate and (*b*) DLC-coated plate

Downloaded 14 Jul 2008 to 130.34.231.209. Redistribution subject to ASME license or copyright; see http://www.asme.org/terms/Terms_Use.cfm

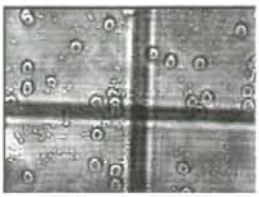

Fig. 6 Behavior of erythrocytes in plasma on MPC-coated plate (F_T=35 pN, F_N=47 pN)

observe a sufficient number of cells we used the 10× objective lens. The normal force was fixed at F_N=47 pN and the tangential force F_T was set at 5 pN intervals between 5 pN and 40 pN using plasma as a medium on the MPC-coated, DLC-coated, and noncoated plates, and at F_T=2.5, 5, 10, 20, 30 pN using saline as a medium on the MPC-coated plate.

Figure 8 is an example of 1 of 100 sequentially captured images for F_T=35 pN using plasma on the noncoated plate. These images were processed by the PTV software to obtain the velocities of cells using two sequential images. The typical number of velocities of cells obtained on the image was 140 in the present work. The mean value and the standard deviation of the velocities of cells obtained in each image are plotted in Figs. 9(*a*) and 9(*b*), respectively. By averaging these data we obtained the mean value and the standard deviation of the cell velocities for one experimental condition.

Figures 10(*a*)–10(*c*) show the mean velocity of cells with the tangential force for the MPC-coated, DLC-coated, and noncoated plates, respectively. The open symbol represents the results for plasma as the medium, while the closed symbol in Fig. 10(*a*) represents the results for saline. Each plot is based on the average value of four measurements of the same blood sample. For the plasma medium, the measurement was performed more than once using the blood of the same person sampled on different days. A pair of plots at the same F_T in a range of 10–40 pN represent the results three months apart. There are no data with saline as a medium for DLC-coated and noncoated plates since all the cells stick to the plates under this condition.

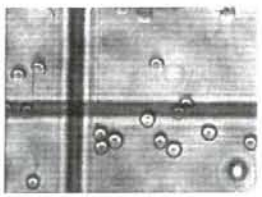

(*a*)

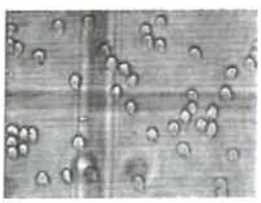

(*b*)

Fig. 7 Behavior of erythrocytes in saline (F_T=30 pN, F_N=47 pN): (*a*) MPC-coated plate and (*b*) DLC-coated plate

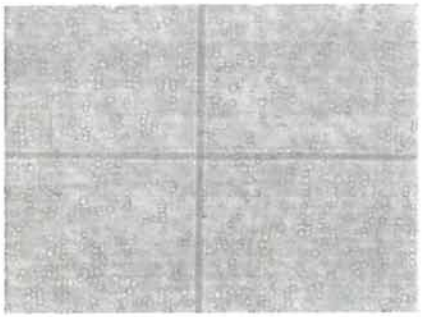

Fig. 8 Behavior of erythrocytes in plasma on noncoated plate (F_T=30 pN, F_N=47 pN).

By introducing the above results into Eq. (3), we obtained the friction force working between the cells and the plate. Equivalent shear rate and gap width were obtained from Eqs. (5) and (6). Figure 11(*a*) shows the friction force and the equivalent shear rate as a function of the mean cell velocity for the MPC-coated, DLC-coated, and noncoated plates in plasma and the MPC-coated plate in saline. Figure 11(*b*) shows the corresponding results for the equivalent gap width.

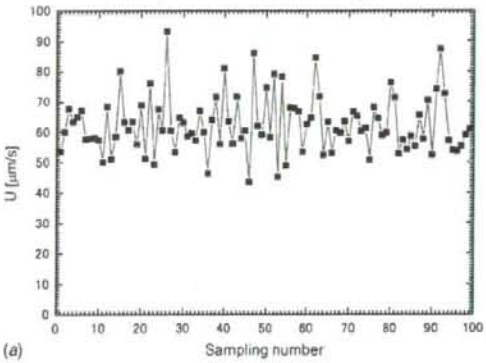

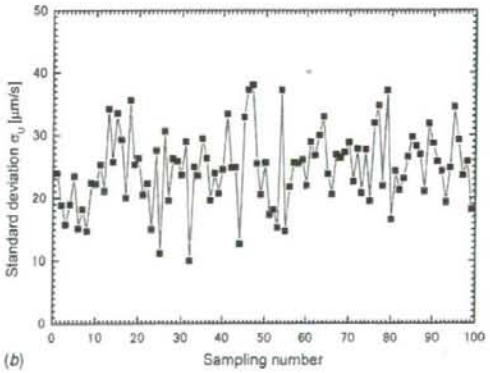

Fig. 9 Variation of mean value and standard deviation of velocity of erythrocytes in plasma on noncoated plate (F_T =30 pN, F_N=47 pN): (*a*) mean value and (*b*) standard deviation

Downloaded 14 Jul 2008 to 130.34.231.209. Redistribution subject to ASME license or copyright; see http://www.asme.org/terms/Terms_Use.cfm

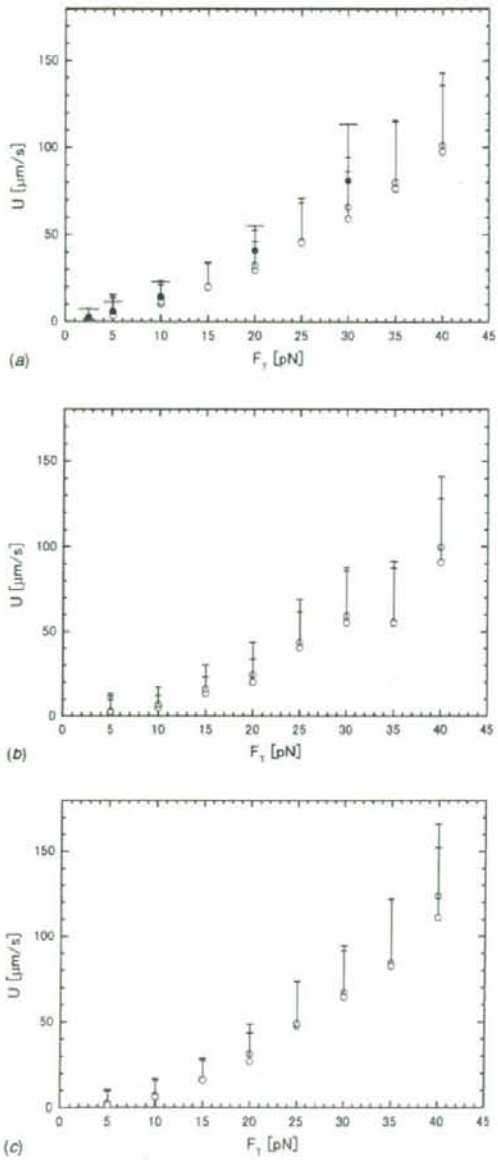

Fig. 10 Cell velocity in plasma with tangential force. Open symbols: plasma; closed symbols: saline; error bar represents standard deviation. (F_N=47 pN): (*a*) MPC-coated plate, (*b*) DLC-coated plate, and (*c*) noncoated plate.

5 Discussion

Under magnification, the typical concave configuration of erythrocytes was clearly observed. It is well known that a tank-treading motion sometimes occurs for erythrocytes in a shear flow [14] or for those moving eccentrically in a capillary [15]. In the present experiment, occurrence of the tank-treading motion was examined in movies by observation of face-on outline of cells. Such observation indicated that the cells move without tank treading motion as the face-on outlines distorted from circular shape do not change during the motion. The centrifugal force is applied to the entire body of each cell, or equivalently to its gravitational center and shear force around the cell balances the centrifugal force. The shear force on the bottom surface of the cell dominates in the total shear force while that on the top surface is small but has the same direction as that of the bottom surface. For a cell in a shear flow, on the other hand, shear forces acting on the top and bottom sides of the cell at the same magnitude and in opposite directions effectively drive the cell into a tank-treading motion. However, a recent study suggests that a tank-treading motion can occur on a cell in a biconcave shape at low shear stress [16]. Therefore, it is necessary to exactly identify the occurrence of tank-treading motion under the present experimental conditions, for example, by marking a certain location on the cell surface with latex spheres in a future study.

The friction characteristics of erythrocytes in plasma using the DLC-coated and noncoated plates are similar changing approximately proportional to the 0.5th power of the cell velocity. The cells stick to the plates when plasma is replaced with saline, implying that plasma protein plays an important role to determine friction characteristics. The results of the MPC-coated plate using plasma are similar to those using the other plates in the range of relatively large cell velocity, but deviate from those with decreased cell velocity. The results change nearly proportional to the 0.75th power of the cell velocity in the range of small velocities less than 10 μm/s. The friction force observed in the MPC-coated plate in saline is similar to that in plasma but somewhat smaller. This means that the friction characteristics of cells using the MPC-coated plate are essentially independent of plasma protein. Therefore, in the range of large cell velocities, in which all the friction characteristics are similar, plasma protein plays a secondary role in determining friction characteristics.

Shear stress in the fluid flow between the cell and the plate should play the essential role to determine the friction force. The cell velocity, the gap width between the cell and the plate, and the viscosity of the fluid are the factors that determine the flow shear stress. The shear rate in the gap ranged between 30 1/s and 700 1/s in a present experiment. It should be noted that the resultant shear force acted only on the bottom surface of the cell to counterbalance the centrifugal force. Therefore, the effect of this shear rate on the cell motion is different from that on a cell in a uniform shear flow. The equivalent gap distance between the cell and the plate ranged between 0.02 μm and 0.2 μm. The results for the MPC-coated plates with plasma and saline were identical. The gap widths for the DLC-coated and noncoated plates were almost the same and were smaller than those of MPC-coated plates. In a previous study [9], we proposed that the distance corresponds to the size of plasma protein, but the present result for the MPC-coated plate with saline invalidates this possibility. Electrochemical force, such as the strong attraction of water molecules on the surface of MPC polymer [11], or hydrodynamic force, such as squeezing force due to the movement of the cell, should be considered to determine the distance, but these considerations go beyond the scope of the present study. The deviation of the friction force and the equivalent gap width of the DLC-coated and noncoated plates from that of the MPC-coated plate in small velocities is probably explained by the effect of additional friction force due to plasma proteins.

In circulatory medical devices, centrifugal force acts on the blood flow in a curved duct or in a turbo pump. In such a case blood cells are forced to move along a device surface under the effect of normal forces. The present findings suggest that friction force acting on the erythrocytes on the MPC-coated plate is smaller than that on the DLC-coated or noncoated plate in the region of small cell velocity. In order to apply these results to the device design, however, further study is necessary, for example, clarification of the effect of normal force or temperature. It is also important to evaluate the normal force acting on blood cells in a

Downloaded 14 Jul 2008 to 130.34.231.209. Redistribution subject to ASME license or copyright; see http://www.asme.org/terms/Terms_Use.cfm

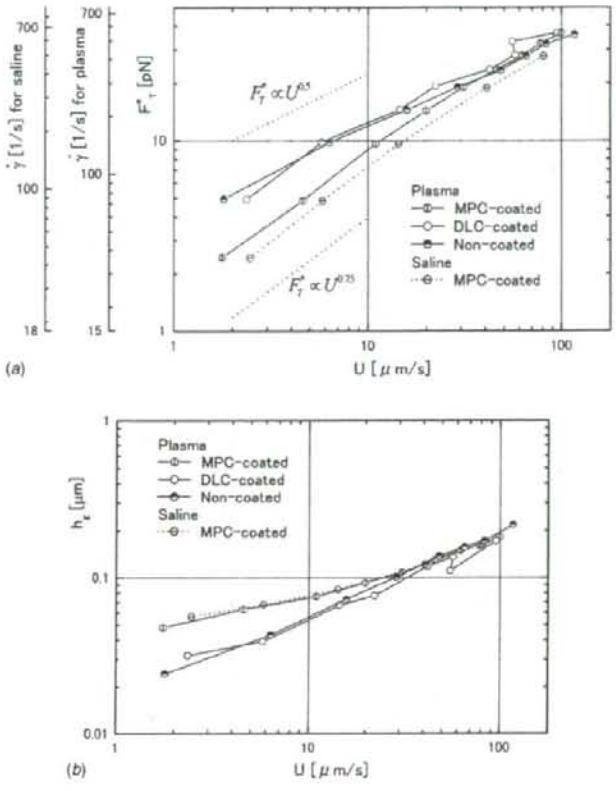

Fig. 11 Friction characteristics of erythrocytes: (*a*) friction and equivalent shear rate and (*b*) equivalent gap width

blood flow. Relating to this problem, although theoretical work has been performed for the Stokes flow impinging on a spherical cap on a plane wall [17], further study must be done. Frictional characteristics between blood cells and device surfaces are important for hemolysis and thrombosis. The present study dealt with the frictional characteristics of erythrocytes in relation to hemolysis in the devices as the first step. For thrombosis in medical devices, consideration of platelets is essential. Application of the present method to platelets and other cells such as neutrophils will be treated in a future work.

In addition, we would like to mention that the friction characteristics of erythrocytes moving along a flat plate under the inclined centrifugal force differ from those of the blood flow in blood vessels. However, the present method provides a fundamental understanding of the frictional characteristics of blood cells, providing a basis upon which a mathematical model of microcirculation can be constructed. For that purpose, measurements using endothelial-cell-cultured glass plates are a natural extension of the present research.

Acknowledgment

The authors acknowledge Professor Toshiyuki Takagi of the Institute of Fluid Science, Tohoku University for his help in making the DLC-coated plates, and Professor Kazuhiko Ishihara of the University of Tokyo for providing MPC polymer and for useful discussions. They wish to thank the staff of Department of Radiology and Health Administration Center, Tohoku University for their assistance in blood sampling. They also thank Mr. Manabu Saito for his help in preparing the manuscript.

References

[1] Schmid-Schoenbein, G. W., 1999, "Biomechanics of Microcirculatory Blood Perfusion," Annu. Rev. Biomed. Eng., **1**, pp. 103–127.
[2] Pries, A. R., Secomb, T. W., and Gaehtgens, P., 2000, "The Endothelial Surface Layer," Eur. J. Physiol., **440**, pp. 653–666.
[3] Secomb, T. W., Hsu, R., and Pries, A. R., 1998, "A Model for Red Blood Cell Motion in Glycocalyx-Lined Capillaries," Am. J. Physiol. Heart Circ. Physiol., **274**(3), pp. H1016–H1022.
[4] Harvey, E. N., and Loomis, A. L., 1930, "Scientific Apparatus and Laboratory Methods," Science, **72**, pp. 42–44.
[5] Inoue, S., Knudson, R. A., Goda, M., Suzuki, K., Nagano, C., Okada, N., Takahashi, H., Ichie, K., Iida, M., and Yamanaka, K., 2001, "Centrifuge Polarizing Microscope. I. Rationale, Design and Instrument Performance," J. Microsc., **201**, pp. 341–356.
[6] Kaneda, I., Kanitsubo, E., and Hiramoto, Y., 1990, "The Mechanical Structure of the Cytoplasm of the Echinoderm Egg Determined by 'Gold Particle Method' Using a Centrifuge Microscope," Dev., Growth Differ., **32**, pp. 15–22.
[7] Kuroda, K., and Kamiya, N., 1989, "Propulsive Force of Paramecium as Revealed by the Video Centrifuge Microscope," Exp. Cell Res., **184**, pp. 268–272.
[8] Tameyasu, T., Akimoto, T., Hirohata, Y., Shirakawa, I., Yamamoto, N., Kosuge, S., and Sugi, H., 1998, "Force-Velocity Relation of Sliding of Skeletal Muscle Myosin Arranged on a Paramyosin Filament on Actin Cables," Jpn. J. Physiol., **48**, pp. 115–121.
[9] Hayase, T., Shirai, A., Sugiyama, H., and Hamaya, T., 2002, "Measurement of Frictional Characteristics of Red Blood Cells Moving on a Plate in Plasma Due to Inclined Centrifugal Force (in Japanese)," Trans. Jpn. Soc. Mech. Eng., Ser.

Downloaded 14 Jul 2008 to 130.34.231.209. Redistribution subject to ASME license or copyright; see http://www.asme.org/terms/Terms_Use.cfm

B, **68**, pp. 3386–3391.
[10] Mohanty, M., Anilkumar, T. V., Mohanan, P. V., Muraleedharan, C. V., Bhuvaneshwar, G. S., Derangere, F., Sampeur, Y., and Suryanarayanan, R., 2002, "Long Term Tissue Response to Titanium Coated With Diamond Like Carbon," Biomol. Eng., **19**, pp. 125–128.
[11] Ishihara, K., Nomura, H., Mihara, T., Kurita, K., Iwasaki, Y., and Nakabayashi, N., 1998, "Why do Phospholipid Polymers Reduce Protein Adsorption?," J. Biomed. Mater. Res., **39**, pp. 323–330.
[12] Schlichting, H., 1979, *Boundary-Layer Theory*, 7th English ed., McGraw-Hill, New York, p. 114.
[13] Cooney, D. O., 1976, *Biomedical Engineering Principles: An Introduction to Fluid, Heat, and Mass Transport Process*, Dekker, New York.
[14] Sutera, S. P., Tran-Son-Tay, R., Boylan, C. W., Williamson, J. R., and Gardner, R. A., 1983, "A Study of Variance in Measurements of Tank-Treading Frequency in Populations of Normal Human Red Cells," Blood Cells, **9**, pp. 485–495.
[15] Fung, Y. C., 1996, *Biomechanics: Circulation*, Springer-Verlag, New York, p. 308.
[16] Fischer, T. M., 2004, "Shape Memory of Human Red Blood Cells," Biophys. J., **86**, pp. 3304–3313.
[17] El-Kareh, A. W., and Secomb, T. W., 1996, "Stokes Flow Impinging on a Spherical Cap on a Plane Wall," Q. J. Mech. Appl. Math., **49**, pp. 179–193.

Downloaded 14 Jul 2008 to 130.34.231.209. Redistribution subject to ASME license or copyright; see http://www.asme.org/terms/Terms_Use.cfm

Breast Cancer (2008) 15:145–152
DOI 10.1007/s12282-008-0037-0

CONFERENCE PAPER

In vivo single molecular imaging and sentinel node navigation by nanotechnology for molecular targeting drug-delivery systems and tailor-made medicine

Motohiro Takeda · Hiroshi Tada · Hideo Higuchi · Yoshio Kobayashi · Masaki Kobayashi · Yuu Sakurai · Takanori Ishida · Noriaki Ohuchi

Published online: 4 March 2008
© The Japanese Breast Cancer Society 2008

Abstract The recent advances in nanotechnology have a great potential to improve the prevention, diagnosis, and treatment of human diseases. Nanomaterials for medical applications are expected to grasp pharmacokinetics and the toxicity for application to medical treatment on the aspect of safety of the nanomaterials and nanodevices. We describe a generation of CdSe nanoparticles [quantum dots (QDs)] conjugated with monoclonal anti-HER2 antibody (Trastuzumab), for single molecular in vivo imaging of breast cancer cells. We established a high-resolution in vivo 3D microscopic system for a novel imaging method at the molecular level. The cancer cells expressing HER2 protein were visualized by the nanoparticles in vivo at subcellular resolution, suggesting future utilization of the system in medical applications to improve drug-delivery systems to target the primary and metastatic tumors for made-to-order treatment. We also describe sentinel node navigation using fluorescent nanoparticles for breast cancer surgery in experimental model, which have shown the potential to be an alternative to existing tracers in the detection of the sentinel node if we select the appropriate particle size and wavelength. Future innovation in cancer imaging by nanotechnology and novel measurement technology will provide great improvement, not only in the clinical field but also in basic medical science for the development of medicine.

Keywords Single molecular imaging · Sentinel lymph node biopsy · Nanomedicine · Breast cancer · HER2

This article is based on a presentation delivered at the Presidential Symposium 1, "Breast cancer: individualized diagnosis for tailored treatment," held on 29 June 2007 at the 15th Annual Meeting of the Japanese Breast Cancer Society in Yokohama.

M. Takeda (✉) · H. Tada · Y. Sakurai · T. Ishida · N. Ohuchi
Department of Surgical Oncology, Graduate School of Medicine, Tohoku University, 1-1 Seiryo-machi, Aoba-ku, Sendai 980-8574, Japan
e-mail: motot@d1.dion.ne.jp

M. Takeda
Department of Bioengineering and Robotics, Graduate School of Engineering, Tohoku University, Aoba 01, Sendai 980-8579, Japan

H. Higuchi
Biomedical Engineering Research Organization, Tohoku University, Sendai, 6-6-11-901, Aramaki, Aoba-ku, Sendai 980-8579, Japan

Y. Kobayashi
Department of Biomolecular Functional Engineering, College of Engineering, Ibaraki University, 4-12-1 Naka-narusawa-cho, Hitachi, Ibaraki 316-8511, Japan

M. Kobayashi
Division of Electronics, Tohoku Institute of Technology, 35-1 Kasumi-cho, Yagiyama, Taihaku-ku, Sendai 982-8577, Japan

Introduction

Tumor targeting anti-cancer therapeutics by conjugating tumor-specific antibodies is of great interest in oncology, pharmacology, and nanomedicine. This approach will allow to increase therapeutic efficacy and to decrease systemic adverse effect [1, 2]. Quantitative investigation of dynamics of such drug delivery in vivo is crucial to enable the development of more effective drug-delivery systems. One of the best ways to perform this is to apply new technology in biophysics that the positions of proteins are detected quantitatively at the single-molecule

level with nanometer precision [3]. However, the specific delivery processes in vivo is not known at the single-particle level. Conventional imaging modalities such as computed tomography, magnetic resonance imaging, positron emission tomography, and organic fluorescence or luminescence imaging have insufficient resolution to analyze the pharmacokinetics of drugs at the single-particle level in vivo [4].

To address this issue, real-time single-particle tracking using quantum dots (Qdots) has been applied to the study of drug delivery. Qdots, fluorescent nanocrystals, were expected to be a good biomarker because of their intense brightness and stability, in contrast to existing organic dyes and GFP [5, 6]. In cultured cells, single-particle tracking has yielded invaluable information on the function of purified proteins [7, 8]. Recent work shows that the antibody-conjugated Qdots have allowed real-time tracking of single-receptor molecules on the surface of living cells [9]. However, no real-time single-particle tracking in live animals has been reported, and it is uncertain if the single particle of Qdots could be observed or tracked in live animals. We analyzed the movement of single functional Qdots in the tumors of mice from a capillary vessel to cancer cells by a highly sensitive measurement system.

The made-to-order treatment for disease is now strongly expected as well as the evidence-based medicine. In the area of surgery, sentinel node navigation surgery is a major method for performing made-to-order surgery for malignancies. Treatments of cancer with minimum invasive surgery without lymph node dissection based on sentinel lymph node (SN) navigation surgery has become a major concern of made-to-order and low-invasiveness medicine. Some radioisotopes and dyes are utilized for SN detection in the standard method, however, each detection method has advantages and disadvantages. To make up for the disadvantages, we aimed at developing a new noninvasive method using nanosized fluorescent beads of uniform size that could efficiently visualize SN from outside the body and perform experiments to determine the appropriate size and fluorescent wavelength and confirm that uniformly nanosized fluorescent beads have the potential to be an alternative to existing tracers [10, 11] in the detection of the SN in animal. These data should be useful in establishing clinical fluorescence measurement methods in the future.

Materials and methods

Single molecular imaging of breast cancer by quantum dots conjugated with anti-HER2 antibody

We made conjugations of Qdot (Quantum Dot Corporation, Hayward, CA) and trastuzumab (Chugai pharmaceutical Co., LTD, Tokyo, Japan) with a Qdot 800 Antibody Conjugation Kit (Quantum Dot Corporation, Hayward, CA) via poly ethylene glycol (M.W. 2000) and heterobifunctional cross-linker 4-(maleimidomethyl)-1-cyclohexanecarboxylic acid N-hydroxysuccinimide ester (SMCC).

The final concentration of Qdots and trastuzumab complexes (QT complexes) was determined by measuring the conjugate absorbance at 550 nm and using an extinction coefficient of 1,700,000 M^{-1} cm^{-1} at 550 nm.

The human breast cancer cell line KPL-4 [12], which overexpresses HER2 and is sensitive to trastuzumab, was kindly supplied from Dr. J. Kurebayashi (Kawasaki Medical School, Kurashiki, Japan). KPL-4 cells were cultured in Dulbecco's modified Eagle's medium supplemented with 5% fetal bovine serum. A suspension of KPL-4 was transplanted subcutaneously to the dorsal skin of female Balb/c nu/nu mice at 6–10 weeks of age (Charles River Japan, Yokohama, Japan). Mice bearing a tumor volume of 100–200 mm^3 were selected for experiments. All operations on animals were in accordance with the institutional animal use and care regulations. This study was approved by Animal Care and Use Committee of Tohoku University.

QT complexes were injected into tail vein of mice. The mice were placed under anesthesia by the intraperitoneal injection of a ketamine and xylazine mixture at a dosage of 95 and 5 mg/kg, respectively. The temperature of mice was maintained at 37°C by a thermo-plate and objective lens heater. The modified dorsal skin fold chamber (DSFC) method [13] was used to fix the exposed mouse tumor on the stage of the microscope. Two sterilized polyvinyl chloride plates (0.5 mm thickness) containing a window were mounted so as to fix the extended double layer of dorsal skin including the tumor site. Skin between chambers sutured with 6-0 nylon around the window, and the tumor could be located in the center of the window and fixed without influence from the beating of the heart and breathing. The tumor was placed surface down on the neutral saline mounted cover slip on a viewing platform of an inverted microscope. The mouse was fixed to a metal plate on the stage designed to stabilize the chamber. Tumors can be visualized directly by means of this setup.

The mice were killed by CO_2 overdose, after imaging. The tumors were removed and divided for histological and immunohistochemical examination. In the histological Qdot uptake study, tumors were frozen and cryosectioned 6 μm thickness, fixed with acetone at 0°C and examined with an imaging system. For immunohistological examination, tumors were fixed in 10% neutral-buffered formalin overnight and then transferred into ethanol before processing and paraffin embedding. Immunohistochemical analysis was performed on paraffin sections at 6-μm

thickness using the HercepTest (Dako Cytomation, CA) to confirm HER2 expression.

As shown in Fig. 1, the optics system for 3D observation consisted primarily of an epi-fluorescent microscope (IX71, Olympus) with modifications, a Nipkow lens type confocal unit (CSU10, Yokogawa) and an electron multiplier type CCD camera (iXon 887, Andor). The confocal unit adopts multi-beam scanning using about a thousand beams that are simultaneously emitted through a pin-hole disk to facilitate high-speed scanning. The EMCCD has advantage that offering unsurpassed sensitivity performance, and has been shown to yield markedly improved SN ratio. The objective lens was moved by a piezo actuator with a feedback loop for stabilizing the position of the focus. A computer controlled the piezo actuator in synchronization with the image acquisitions in order that the objective lens remained within the exposure time of the CCD camera. An area of 30 × 30 μm^2 was irradiated by a green laser (532 nm, Crystalaser).

The *xy*-position of the fluorescent spot was calculated by fitting to a 2D Gaussian curve. The single molecule could be identified by the fluorescence spot, and quantitative and qualitative information such as velocity, directionality, and transport mode was obtained using time-resolved trajectories of particles. The resolution of the position was determined from the position of immobile QT complexes in a chemically fixed tumor cell. The resolution of the *x* and *y* directions of images taken at an exposure time of 33 ms was 30 nm, taking into consideration the standard deviation.

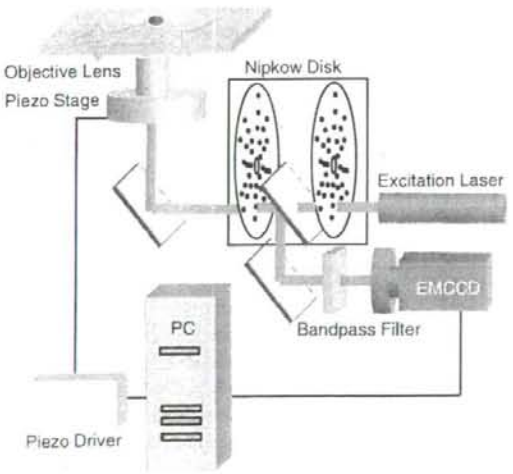

Fig. 1 The 3D intravital imaging system for visualization of QT complexes in a mouse

Sentinel node navigation by nanosized fluorescent beads

We employed "FluoSpheres®" manufactured from high-quality polystyrene microspheres (Molecular Probe Inc, OR, USA) for sentinel node detection. We selected beads of sizes 20, 40, 100, and 200 nm, and fluorescent colors of yellow–green (YG) (excitation/emission maxima at 505/515 nm), dark red (DR) (660/680 nm), far red (FR) (690/720 nm) and infrared (IR) (715/755 nm). The size of beads is very homogeneous, 0.02 ± 0.004 μm in 20-nm size and 0.1 ± 0.005 μm in 100 nm. We designed a laser scanning fluorescence detection system that consists of three lasers, a resonant scanner (resonant frequency/200 Hz), a rotational pulse-stage and a CCD camera (Fig. 2). We used a diode pumped solid-state blue laser (473 nm, 7 mW) as the excitation source of YG fluorescent beads. For excitation of DR, FR, and IR fluorescent beads, we used a He-Ne laser (632.8 nm, 14.6 mW) or a laser diode (657 nm, 3.56 mW). The inguinal and femoral areas were continuously irradiated and scanned over an area of 30 x 50 mm. The fluorescence image was observed using a CCD camera (XC-EI50, Sony) with an optimum band-pass filter for each fluorescent bead.

In addition, the spectrum of scanned area was analyzed with a spectrometer. Under ether anesthesia, the hair of rats' lower body was removed to avoid autofluorescence of it. Then 50 μl of FluoSpheres® 2% w/v suspension was subcutaneously injected at the footpad of the hind leg. Spectral analysis of fluorescence from rats injected with beads was performed to clarify the signal-to-noise ratio of fluorescence from beads and autofluorescence. After observation from outside the body (through the skin) for 30–180 min, we peeled back the skin at the subcutaneous layer and ascertained the area of lymph nodes with navigation of their specific fluorescence. Then, the lymph nodes were removed and fixed with formalin for histological observation to confirm that the tissue was a lymph node.

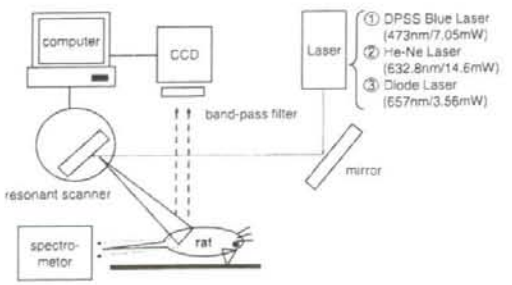

Fig. 2 Fluorescence imaging system for sentinel node detection using nanosized particles